Environmental Modeling

Dissolution of complex metal oxides from first-principles and thermodynamics: Cation removal from the (001) surface of Li(NiMnCo)O

Joseph Bennett, Diamond Jones, Xu Huang, Robert J Hamers, and Sara E. Mason

Environ. Sci. Technol., **Just Accepted Manuscript** • DOI: 10.1021/acs.est.8b00054 • Publication Date (Web): 13 Apr 2018

Dissolution of complex metal oxides from first-principles and thermodynamics: Cation removal from the (001) surface of $Li(Ni_{1/3}Mn_{1/3}Co_{1/3})O_2$

Joseph W. Bennett[1], Diamond Jones[1], Xu Huang[1], Robert J. Hamers[2] and Sara E. Mason[1]**

1: Department of Chemistry

University of Iowa, Iowa City, Iowa 52242;

2: Department of Chemistry

University of Wisconsin-Madison, Madison, WI 53706

E-mail: sara-mason@uiowa.edu

*To whom correspondence should be addressed

Abstract

The rapid increase in use of Li-ion batteries in portable electronics has created a pressing need to understand the environmental impact and long-term fate of electonic waste (e-waste) products such as heavy and/or reactive metals. The type of e-waste that we focus on here are the complex metal oxide nanomaterials that compose Li-ion battery cathodes. While in operation the complex metal oxides are in a hermetically sealed container. However, at the end of life, improper disposal can cause structural transformations such as dissolution and metal leaching, resulting in a significant exposure risk to the surrounding environment. The transformations that occur between operational to environmental settings gives rise to a stark knowledge gap between macroscopic design and molecular-level behavior. In this study we use theory and modeling to describe and explain previously published experimental data for cation release from $Li(Ni_{1/3}Mn_{1/3}Co_{1/3})O_2$ (NMC) nanoparticles in an aqueous environment (*Chem. Mater.* **2016** (28) 1092-1100). To better understand the transformations that may occur when this material is exposed to the environment, we compute the free energy of surface dissolution, ΔG, from the complex metal oxide NMC for a range of surface terminations and pH.

Introduction

Complex metal oxides (CMOs) have transformed the way in which technology is used worldwide, with an extensive, ever-increasing number of applications being discovered on an almost daily basis (*1*). Nanoscale CMOs have been incorporated into energy production technologies, form the basis of contaminant remediants (*2*, *3*), and can be found in widespread commercially available items such as sunscreen, or in electric vehicles, where they constitute a majority of the electroactive components of a Li-ion battery (*4–6*). Recent studies have postulated that the large scale industrial production and subsequent use of CMOs may lead to inadvertent releases of CMOs into the environment, and that these exposures may be problematic in the immediate future (*7*). A key example here is that there is no forseeable economic benefit or globally regulated system in place

to recycle electronic waste ("e-waste") such as spent Li-ion batteries (*8*). Even though research has shown that the toxicants associated with CMOs from discarded electronic devices can leach into the environment and pose a serious risk to human health (*9*), there is no (inter)national infrastructure for recycling lithium-ion batteries. This is especially problematic for the developing countries (with less stringent environmental regulations) to which a majority of our e-waste is shipped.

The environmental and biological impact of nanoscale CMOs are largely unknown (*10–12*), and this has resulted in one of the grand challenges of modern chemistry. In response, investigations at the nano-bio interface have emerged, where "safe-by-design" research has focused on how to optimize or maintain nanomaterial-based device performance while minimizing adverse biological impact (*13–15*). To address the negative biological impacts that result from exposure, and to align closely with the principles of green chemistry (*16*), the nano-bio community has called for safer, sustainable design rules across all stages of the life cycle of the CMOs.

One looming problem remains: there is still a large fundamental knowledge gap in designing and developing sustainable nanotechnology, and that is the ability to predict the properties of CMOs as a function of environmental changes. Nanoscale CMOs have a high surface to volume ratio and exhibit reactivities that depend strongly upon their local chemical surroundings. It has been demonstrated that properties such as (hetero)agglomeration can be controlled in aqueous media as a function of pH, ion species, and ionic strength (*17*, *18*). This also implies that CMOs are able to react to and transform rapidly with changes in their surroundings (*19*, *20*), and that the fate, transport and toxicology of transformed CMOs are most times unidentified. The lack of molecular understanding of nanoscale CMOs transformations is noted as a weakness in nano Environmental Health and Safety (nanoEHS) (*21*), and there is a need to isolate the set(s) of parameters that govern nanoscale CMO transformations.

First-principles DFT has already led to a revolutionary development of the CMO materials that compose a Li-ion battery (*22–33*), specifically the cathode materials (*34–38*). The interplay of computable information (*39–42*) and experimental endeavors has resulted in a booming industry (*43*, *44*). While DFT-based research has broadly impacted materials design (*45–49*), the

complexity and heterogeneity of CMOs in the environment complicates the direct application of electronic structure methods. However, by using DFT in conjunction with thermodynamic modeling, the effects of finite pressure and temperature conditions and macroscopic properties can be taken into account to understand the nanoscale transformations of CMOs that accompany changes in the chemical environment.

Analyses that combine DFT and thermodynamics can be used to elucidate how changes in environmental conditions will result in changes in CMO surface structure, and hence reactivity. A recent example of how this was applied to the CMO $LiCoO_2$ (LCO) demonstrated that comparing the results of an atomistic thermodynamic surface free energy analysis to a general DFT + solvent ion model based on Hess's Law (*50*) showed that two different surface terminations dominate the experimentally/environmentally relevant portions of the LCO phase-diagram (*51*), either a Li or H-terminated surface. Under ambient hydrated conditions, Li will exchange for H (from water) to create surface OH bonds. The interpretation is that there is a thermodynamic driving force for surface Li to dissolve, and ultimately be replaced by water products (H or OH abstracted from an aqueous solution) on the surface. In showing that it was favorable for Li to dissolve from LCO, the modeling agrees with the experimentally observed dissolution trend (Li $>$ Co) of LCO nanomaterials (*52*, *53*) as determined by non-linear optical studies.

$Li(Ni_{1/3}Mn_{1/3}Co_{1/3})O_2$ (NMC) (*54–58*), a compositionally tuned variant of LCO, is a CMO that is a likely candidate for large-scale commercialization and deployment in electric vehicles. This makes it a candidate material for increased environmental exposure during its fabrication, operation, and disposal. Recent work on biological-CMO interactions using NMC flakes (of 7 transition metal-oxide (TM-O) layer thickness) has shown that NMC has a negative impact; exposure to 5 mg/L concentrations impaired *Shewanella oneidensis* MR-1 bacterial growth (*59*), and 1 mg/L concentrations interrupted the reproduction and survival of *Daphnia Magna* (*60*). Exposure studies demonstrated that the toxicity can be related to the dissolution of Ni and Co cations from NMC, and that the dissolution is time-dependent. Measurements of dissolved ion concentration showed that much more Li and Ni dissolved out of NMC than Co and Mn for the entire range of

times investigated. Therefore, the trend in dissolution rates is Li $>$ Ni $>$ Co$\approx$Mn (*59*, *61*).

In this study we aim to elucidate the thermodynamic driving force behind the incongruent dissolution of NMC, with an overarching goal of providing molecular-level insight and chemical guidance to the redesign of CMOs with reduced biological impact. We adapt a combined DFT + thermodynamics approach to compute the free energy (ΔG) of dissolution of TM from NMC. We establish a correlation between our computed ΔG to the observed dissolution rate trends. Beyond establishing strong connections to, and interpretations of, experimental dissolution results, we go on to provide information from our theoretical calculations to guide future experiments. Specifically, we systematically vary surface lithiation and hydrogen coverage, and transition metal vacancy densities to provide insight into how these variables affect or control dissolution. Our NMC dissolution study provides computationally derived rules for CMO redesign to mitigate negative impact at the nano-bio interface.

Materials and Methods

Periodic DFT calculations (*62*, *63*) of bulk and surface structures are performed using the open source Quantum Espresso software package (*64*). Each atom is represented using ultrasoft GBRV-type pseudopotentials (*65*, *66*). All calculations use a plane-wave cutoff of 40 Ry for the wavefunction and 320 Ry for the charge density. All atoms are allowed to relax during structural optimizations, and the convergence criteria for the self-consistent relaxation was a maximum residual force of 5 meV/ per atom. Calculations are performed at the GGA level (*67*), unless otherwise noted.

The bulk NMC cell is a $(\sqrt{3} \times \sqrt{3})\mathrm{R}30^{o} \times 2$ modification of a hexagonal LCO primitive cell. LCO belongs to the $NaFeO_2$-Delafossite structure type, and is described in previous studies (*28*, *51*). The bulk NMC cell contains 6 transition metal oxide layers (O-TM-O). To create NMC from LCO, a substitution of 1/3 of the Co^{3+} for Ni^{2+} and 1/3 of the Co^{3+} for Mn^{4+} is made in a perfectly alternating manner that adheres to the trigonal symmetries of the delafossite structure

type and maintains charge neutrality. The transition metal (*TM*) ordering in each layer is shown on the left hand-side of Figure 1, and a condensed version of the vertical direction is shown on the right-hand side of Figure 1. A 6×6×1 *k*-point grid (*68*) is used for calculations of the bulk NMC structure.

The bulk NMC cell is used to generate surface slabs. Prior experimental work (*59*) described the NMC as nanosheets with at least 7 (O-*TM*-O) layers, which would be computationally expensive using DFT methods. Therefore, the surface slabs generated here have 4 total transition metal oxide layers, of which the 2 exterior and 2 interior are related by inversion symmetry, respectively. Each layer contains 3 *TM* sites. To create supercells of these slabs one can multiply cell dimension *a* by integers *n*=2,3, etc. Here, the surface slabs are multiplied by 2 to obtain reference slabs; $2\sqrt{3} \times \sqrt{3}$ supercell slabs are able to support 1/2 coverage of either Li or H, denoted as NMC_{h-Li}, and NMC_{h-H}, respectively. Each contains 6 total *TM* sites per layer so removal of 1 *TM* from these slabs results in a *TM* vacancy density of 16.67%. These half-coverages, shown in Figure 2, are charge neutral, and for the NMC_{h-Li} and NMC_{h-H} slabs, a 3×6×1 *k*-point grid is employed for all calculations.

To obtain dissolution data for lower *TM* vacancy densities (of ≈ 11%), the cell dimension *a* is multiplied by 3 to obtain 9 total *TM* sites within each of the 4 (O-*TM*-O) layers in the slab. For this $3\sqrt{3} \times \sqrt{3}$ slab, a 2×6×1 *k*-point grid (*68*) is used for all calculations. Each *TM* vacancy calculation employs a top-down dissolution model, where the atoms in the layers above the *TM* are dissolved (removed) in addition to the *TM*. For example, to compute the free energy of dissolution of Ni from a hydrated surface, a surface HO above the Ni is removed in addition to the Ni.

A DFT + Solvent Ion method based on Hess's Law (*50*, *69*) employed in previous work on LCO (*51*), is used to compute the change in free energy of dissolution, ΔG. In this method, the computed energies of the reactants and products (ΔG_1) are combined with experimental data (ΔG_2) to obtain the overall ΔG. $\Delta G_1 = E_{products}$-$E_{reactants}$, and zero-point energy (ZPE) correction terms are added to the DFT total energies of NMC slabs as detailed previously (*51*). Based on the Nernst equation, $\Delta G_2 = \Delta G^0_{SHE} - n_e e U_{SHE} - 2.303 n_{H^+} kT\ pH + kT\ ln\ a(H_xAO_y)^{z-}$, where ΔG^0_{SHE} is the

free energy of formation at standard state, relative to the standard hydrogen electrode, eU_{SHE} is the applied potential, relative to the standard hydrogen electrode, and $a^{z-}_{H_xAO_y}$ are the concentrations of the dissolved constituent ions (assumed to be 1×10^{-6}M). n_e and $n_{\mathrm{H^+}}$ are the number of electrons and protons involved in the chemical reactions required for surface dissolution, and are located in Table S1 of the Supplemental Material. Values of $\Delta G^0_{\mathrm{SHE}}$ are taken from Ref. (*70*). At conditions of $eU_{\mathrm{SHE}} = 0$ and $a = 1\times10^{-6}$M, DFT-calculable Pourbaix diagrams (*71*) show that $\mathrm{Ni}^{2+}_{(\mathrm{aq})}$ will be the preferred state of Ni in solution until $\approx$ pH = 9.5 when $\mathrm{NiO}_{(\mathrm{s})}$ will form, $\mathrm{Mn}^{2+}_{(\mathrm{aq})}$ will be dominant until $\approx$ pH = 10, when $\mathrm{Mn_2O_{3(s)}}$ or $\mathrm{Mn_3O_{4(s)}}$ will form, and $\mathrm{Co}^{2+}_{(\mathrm{aq})}$ will be dominant until pH = 7, where $\mathrm{HCoO}^{-1}_{2(aq)}$ becomes the preferred aqueous species. One of the main objectives of this work is to investigate the dissolution of NMC battery material for a range of environmentally relevant conditions, and choosing a pH range from 1 to 9 will allow for dissolution comparisons of the divalent *TM* cation species Ni^{2+}, Mn^{2+}, Co^{2+}. Example calculations of ΔG for dissolution from $\mathrm{NMC_{h-Li}}$ and $\mathrm{NMC_{h-H}}$ slabs are presented in Section S1 of the Supplemental Materials.

The electronic band structure and projected density of states (PDOS) of the bulk material and each surface slab are computed to obtain metrics on how varying surface stoichiometry will affect the behavior of the *TM*. NMC is a redox active material and changes to the surface states will affect the oxidation state and bond lengths of each species. Also investigated are the effects of applying a range of Hubbard *U* (*72–75*) to the *TM* to determine how the addition of this on-site corrective term affects the dissolution properties of a CMO material such as NMC. These comparisons can be found in Section S2 of the Supplemental Materials.

Results and Discussion

Bulk and Surface Models

Figure 1 shows a top view of a (O-*TM*-O layer) in bulk NMC $\sqrt{3}\times\sqrt{3}$ R30^0 $\times$ 2 cell (left hand side), and a side view of the layer ordering in the primitive cell (right hand side). Each *TM* is octahedrally bound in a perfectly alternating manner, and each octahedral unit is edge-sharing;

this connectivity forms a rigid O-*TM*-O layer, and Li is found in the space between these rigid layers. The DFT relaxed bulk NMC has lattice constants *a*=2.883 Å, *c*=14.232 Å, close to the reported bulk lattice constants of a=2.86 Å (+0.80%), c=14.227 Å (+0.04%) from neutron and x-ray refinement data (*76*, *77*), and in line with previous DFT-GGA studies (*41*). Also shown in the right hand side of Figure 1 are $d1$ and $d2$, which describe vertical O-*TM*-O and O-Li-O distances. In DFT-relaxed bulk NMC, these are 2.12 and 2.62 Å respectively, and these bulk values will be compared to surface bond distances later on in the manuscript.

The bulk NMC cell includes magnetic interactions that can be described as ferrimagnetic spin coupling. Low spin Co^{3+} (d^6) has no net spin, but Ni^{2+} (d^8) and Mn^{4+} (d^3) have 2 and 3 unpaired electrons, respectively, that are antiferromagnetically coupled. In this work, Ni^{2+} is spin down and Mn^{4+} is spin up, which leaves an unpaired spin up electron per formula unit of NMC. The left hand side of Figure 3 shows the spin character within the PDOS for each of the *TM* in bulk NMC. The PDOS shows that the highest occupied molecular orbital (HOMO) is composed of bonding states that contain significant contributions from spin-down 3*d* states of Ni (and Co) and the LUMO is composed of anti-bonding states that contain significant contributions from spin-down Mn, the empty 3*d*-states of Mn^{4+}. The identity and location of 3*d* orbitals in the PDOS supports the proposed order of oxidation of redox active transition metals in NMC under standard battery operating conditions. As reported in Ref (*41*), the lithiation state (x_{Li}) of NMC dictates the oxidation state of the *TM*: as Li de-intercalates from between the rigid O-*TM*-O layers, the successive oxidation steps are approximately as follows a) $Ni^{2+} \rightarrow Ni^{3+}$ ($0.67 < x_{Li} < 1$) before b) $Ni^{3+} \rightarrow Ni^{4+}$ ($0.33 < x_{Li} < 0.67$) before c) $Co^{3+} \rightarrow Co^{4+}$ ($0.33 < x_{Li} < 0$). Mn^{4+} remains mostly redox inactive for the range of $0 < x_{Li} < 1$.

The PDOS of the transition metals on the left hand side of Figure 3 is compared to the full electronic band structure of bulk NMC (right hand side of Figure 3). The computed (indirect) band gap (E_{gap}) of NMC is 1.2 eV, close to the value of 1.4 eV reported for LCO (*51*). Inspection of the electronic band structure also shows that both the HOMO and LUMO have minimal dispersion, indicative of the delocalized charge density of redox active transition metals in an edge-sharing

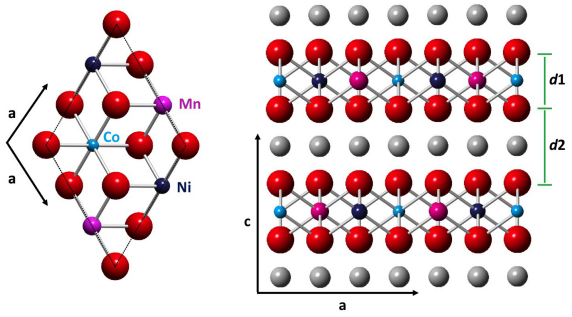

Figure 1: (Left) Top view of a transition metal oxide layer of the $\sqrt{3} \times \sqrt{3}$ R30^0 bulk NMC cell. (Right) Side view of the layer ordering in NMC, with layer spacings $d1$ (O-TM-O) and $d2$ (O-Li-O). The TM are depicted as follows: Ni is dark blue, Co is cyan, and Mn is magenta. Li is depicted as gray and O is red.

scheme.

Given that experimental syntheses of nanoscale NMC materials shows the formation of nanosheets (*59*) that expose primarily (001) faces, and that one of the most thermodynamically stable surfaces for related materials (LCO) is the polar (001) surface (*42*, *51*), the focus of the following work will be on the (001) surface of NMC.

Shown in Figure 2 are side and top views of the NMC$_{h-Li}$ and NMC$_{h-H}$ surfaces. Li resides above a three-fold hollow site on the (001) surface, which is a continuation site where it would appear in the bulk structure. H, however, is directly above an O atom. This is different from the location of surface Li and creates an OH surface bond. To fully understand how surface terminations dictate dissolution trends, the effects of Li and H surface coverages ranging from 0 (oxide terminated) to 2/3 are investigated. This range of non-stoichiometric surface terminations may be present under a variety of variable environmental conditions, and away from ultrahigh vacuum conditions surfaces terminated with water products are expected to be dominant.

Table 1 presents bond distances for the relaxed supercell slabs surface structures in this study. The bond distance for O-$TM-O$ ($d1$), for the range of Li and H-terminated (001) surfaces from 0 to 2/3, increases from 1.98 to 2.12 Å with an increase in surface coverage of either H or Li. The value of $d1$ at higher coverage, 2.12 Å is the same as the bulk value. This indicates that for lower surface coverages it is more likely that that the TMs are oxidized relative to full Li occupancy

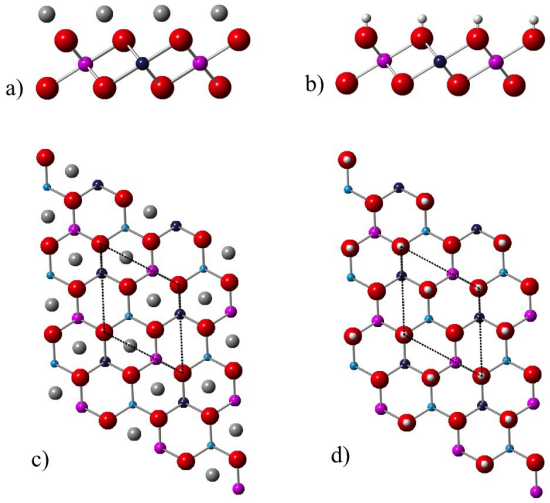

Figure 2: Comparison of the side (and top) views of the surface layer of NMC for a) (c) NMC_{h-Li} and b) (d) NMC_{h-H}. Li is above a three-fold hollow surface site and H is directly above an O in the surface layer, forming an OH bond.

of the ground state. Given the *TM* redox step behavior of NMC presented earlier in the Results section, the most likely species to oxidize will be Ni^{2+}; Co^{3+} and Mn^{4+} are likely to remain redox inactive for the range of surface terminations investigated here.

For surfaces with 1/3 to 2/3 Li-coverage, there is an increase in Li-O bond distance from 0.83 to 1.00 Å, as Li coverage increases. Compared to one-half of the bulk distance *d*2, 1.31 Å, these values are significantly shorter, indicating that surface Li are held more tightly to the surface than in the bulk. This decrease in Li-O bonds for different Li-coverages is opposed to H-terminated surfaces between 1/3 and 2/3 coverage, where OH bonds are uniformly 1.00 Å. These results indicate that the tunability of chemical environment via surface terminations has a direct impact on the bond lengths and oxidation state of the surface transition metals, and for the range of terminations investigated here, yield demonstrable changes in bond length that should be experimentally verifiable.

The change in O-*TM*-O bond lengths as a function of surface termination can be correlated to changes in the electronic structure. In Figure 4, the PDOS of the 3*d*-orbitals of Ni in the surface layer of NMC shift with changes in surface termination. The bare oxide surface has a large peak at the Fermi level (E_F), that decreases at 1/3 H-coverage, and then is eventually absent at 2/3 H-

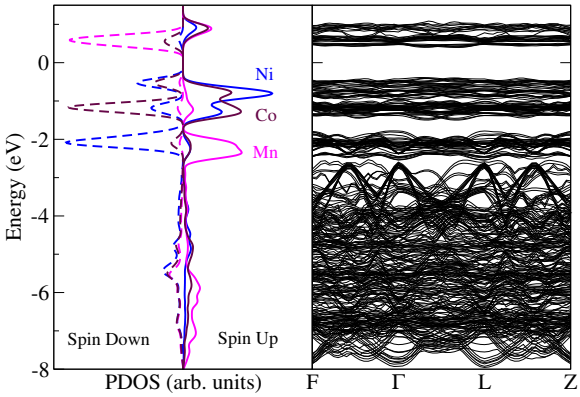

Figure 3: Projected density of states (PDOS, left-hand side) of the *TM* 3*d*-states in bulk NMC and the full electronic band structure (right hand side) of bulk NMC. The HOMO is localized on bonding states that contain significant contributions from Ni and Co and the LUMO is localized on anti-bonding states that contain significant contributions from Mn. E_F is set to zero for both plots.

coverage. The peaks shifts are indicative of the transition between a metallic Ni^{3+}, with partial electron occupancy both above and below E_F, to an insulating Ni^{2+} with full occupancy only below E_F. A change in chemical environment, via surface coverage, causes the reduction of Ni^{3+} to Ni^{2+} in the surface layer of NMC.

Table 1: Surface oxide bond distances for the structures studied here. Shown here are the bond distances for the O-*TM*-O in both the Li and H-terminated surfaces, the Li-O bonds in Li-terminated surfaces, and the H-O bonds in H-terminated surfaces.

surface coverage	O-TM-O H-term	Li-term	O-Li	O-H
0	1.98	1.98	-	-
1/3	2.02	2.08	0.83	1.00
1/2	2.05	2.10	0.93	1.00
2/3	2.12	2.12	1.00	1.00

Dissolution From NMC_{h-Li}

To model dissolution of *TM* from the (001) surface of NMC_{h-Li}, a top-down removal model is considered. Depicted in Figure 5 is a simplified illustration of a possible pathway to removing transition metals from the NMC surface. While the figure shows the step-wise removal of a) Li, b) O, and c) *TM*, this may not be the dissolution pathway taken by these materials. This is why the

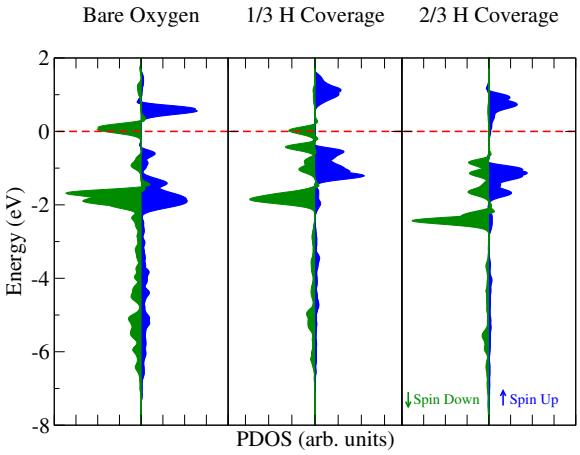

Figure 4: PDOS of the 3*d* states of Ni in the surface layer of NMC, for different H-coverages. The majority spin (down) is green, the minority spin (up) is blue, and the E_F is a dashed red line. The shift in the PDOS indicates a change in oxidation state of Ni as surface coverage changes; Ni^{3+} reduces to Ni^{2+} from 0 to 2/3 H-coverage.

Hess's Law approach described in the Methodology section is crucial; the model only requires the DFT total energies of the initial and final state since ΔG of dissolution is path independent.

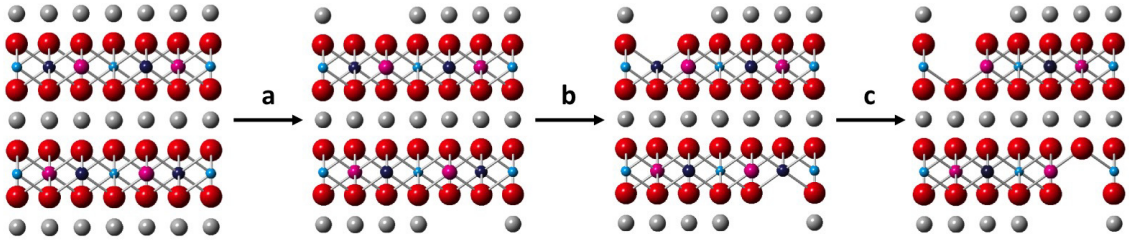

Figure 5: Shown here is an example of the top down mechanism of atom removal employed in the present study. In this depiction, dissolution is from a Li-terminated surface; it requires successive removal of Li, O, and *TM* from the NMC surface.

Dissolution of *TM* from NMC_{h-Li} requires removal of a surface Li, one of the three O that it is connected to in the hollow site, and then a surface *TM* (Figure 5). For the NMC_{h-Li} supercell slab, removal of 1 out of 6 surface *TM*s creates a surface *TM* vacancy density of 16.6%, and the resulting structure is denoted as NMC_{Li-vac}. This dissolution pathway is expressed through the chemical reaction: $NMC_{h-Li} \rightarrow NMC_{Li-vac} + 2TM^{2+} + 2Li^{+} + 2O^{2-}$, which yields an overall expression for ΔG:

$\Delta G = [E_{Li-vac} + 2E_{TM^{2+}} + 2E_{Li^{+}} + 2E_{O^{2-}}] - E_{h-Li} + 2\Delta G_2^{TM^{2+}} + 2\Delta G_2^{O^{2-}} + 2\Delta G_2^{Li^{+}}$. Here, reported

values are divided by 2 to be per surface, and are reported in Table 2.

Li removal is pH independent since it does not require removal of either an O or H, but concerted removal of Li-O-*TM* is pH dependent. This is shown in Figure 6, where ΔG_{Li} is -1.82 eV for the entire range of pH, and ΔG of Ni, Co, and Mn increases as pH increases from 1 to 9. The exception here is the discontinuity of Co at pH=7, where the stable aqueous Co species switches from Co^{2+} to $HCoO_2^-$. ΔG values show that dissolution of Li and Ni from a Li-terminated surface will occur for the full range of pH, while Mn^{2+} will not, since ΔG of Mn^{2+} dissolution is positive for the full range of pH. Co^{2+} dissolution is predicted to occur only at low pH values (below pH = 3.78) while $HCoO_2^-$ dissolution may occur at pH > 7.

The predicted dissolution trend here is Li $>$ Ni $>$ Co $>$ Mn, but for the range of $3.8 <$ pH < 7, only Li and Ni are predicted to dissolve. This correlates to prior experiments, where the majority of initial dissolution products from NMC were Li and Ni, and dissolution of Co and Mn increased at a later point in the expe

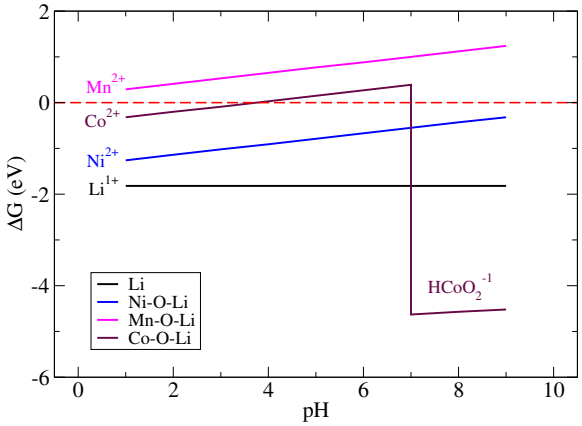

Figure 6: ΔG of dissolution from a the NMC_{h-Li} surface for pH 1 to 9. ΔG of Li is depicted as a solid black line, Ni is dark blue, Co is maroon, and Mn is magenta. A dashed red line is at ΔG=0 for the pH range. Above pH = 7, Co is stable as $HCoO_2^{-1}(\mathrm{aq.})$ and not $Co^{2+}(\mathrm{aq.})$.

Dissolution From NMC_{h-H}

After immersion in aqueous media, it is likely that surface lithium will exchange with water products to yield a hydroxylated (001) surface since the dissolution of Li is thermodynamically fa-

vorable from the (001) surface of NMC. It is of note that exchange of cations on the (001) NMC surface is not necessarily guaranteed a 1:1 exchange, which is why DFT modeling efforts presented here focus on a range of H-terminations from 1/3 to 2/3 H-coverage.

TM removal from a hydroxylated (001) surface may be energetically favorable when compared to the lithiated surface because Li dissolution and OH bond formation are exothermic processes. The dissolution process then becomes a two-step reaction: Li and H exchange occurs before HO-*TM* removal. The example below is for exchange between NMC surfaces, NMC_{h-Li} and NMC_{H}, before *TM* removal.

Step 1: $NMC_{h-Li} + 6H^{+} \rightarrow NMC_{h-H} + 6Li^{+}$

Step 2: $NMC_{h-H} \rightarrow NMC_{H-vac} + 2TM^{2+} + 2H^{+} + 2O^{2-}$, where

$\Delta G = [E_{h-vac} - E_{h-Li}] + 2E_{TM^{2+}} - 4E_{H^{+}} + 2E_{O^{2-}} + 6E_{Li^{+}} + 2\Delta G_2^{TM^{2+}} - 4\Delta G_2^{H^{+}} + 2\Delta G_2^{O^{2-}} + 6\Delta_2^{Li^{+}}$,

and ΔG is divided by 2 to yield the dissolution per side, as described in the previous example.

The thermodynamic driving force for *TM*-OH removal is the dissolution of Li that results from the proton and lithium exchange. When compared to dissolution from the NMC_{h-Li} surface, ΔG dissolution from NMC_{h-H} has decreased. As shown in Table 2, dissolution of Co from NMC_{h-H} is predicted to be favorable at low pH, whereas it was not predicted to occur from NMC_{h-Li}. Figure 7a depicts the ΔG of dissolution of *TM* from the NMC_{h-H} surface. The dissolution trend is Ni $>$ Co $>$ Mn, which was also observed in the Li-terminated surface. Different from the Li-terminated surface is that dissolution of both Ni and Co are predicted to be favorable for the pH range of 1 to 5.9, and that Mn may dissolve as well, even if only at pH $<$ 1.95.

The dissolution of cations from NMC leads to chemical transformations in which reactive oxygen species (ROS) were measured *in situ* in prior experiments (*59*). While the ROS probe used for the initial NMC dissolution experiments was selective towards hydroxyl (OH) radicals, the identity of other potential ROS are still under investigation (*61*), as are the exact roles that ROS may have in the negative biological impact of NMC. To investigate the energetics of different oxygen-containing species mediating *TM* dissolution from the NMC_{h-H} surface, the ΔG of dissolution for removing neutral H_2O molecule is computed. The trends of H_2O mediated *TM* dissolution are

shown in Figure 7b. Depicted as dashed lines, when compared to *TM*-OH dissolution, shown as solid lines, it is obvious that removing H_2O from the surface as a route for *TM* dissolution is not as energetically favorable as OH removal. The difference in dissolution energy between OH and H_2O assisted dissolution supports the claim that removal of *TM* from the NMC surface produces ROS (*59*).

A comparison of ΔG of dissolution for Ni, Co, and Mn at pH = 3 and pH = 6 for all surface *TM* vacancy densities of 16.67% (1/6 cation removal) is presented in Table 2. In all cases Ni dissolution from the (001) surface of NMC is predicted to be preferred relative to dissolution of Co and Mn. One reason could be that Ni^{2+} prefers to be in a square-planar configuration and not the octahedral configuration of the O-*TM*-O units found in the Delafossite structure type. This could also be why Ni dissolution is less sensitive to changes in the chemical environment than either Mn or Co, as it will dissolve under all conditions investigated here because of its preference for forming fewer bon

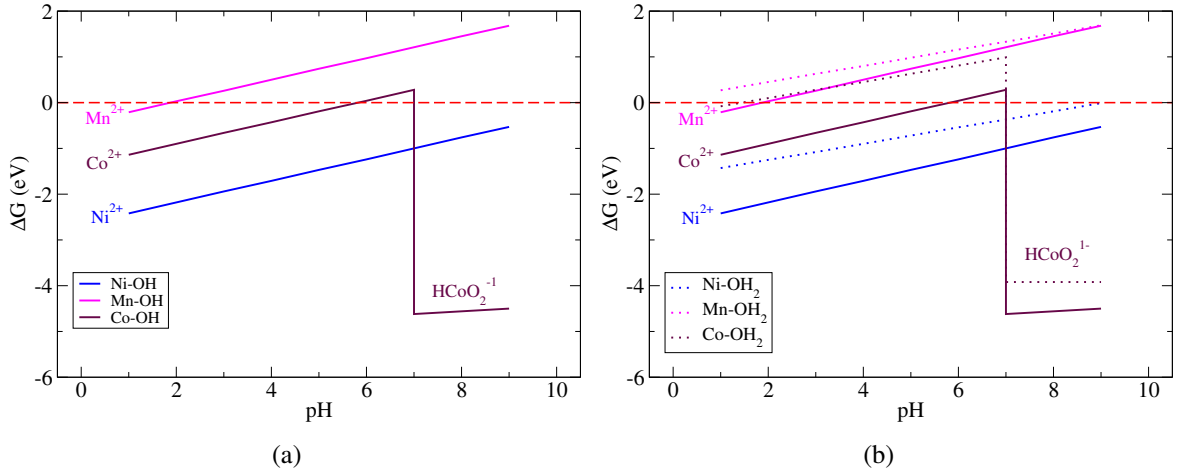

Figure 7: Same color scheme and axes as Figure 6 for ΔG of a) *TM*-OH (solid lines) and b) *TM*-H_2O (dashed lines) removal. Removal of OH is preferred over H_2O for Ni, Co, and Mn for the pH range of 1 to 9.

Table 2: Comparison of ΔG of TM dissolution for each of the 3 removal schemes. All ΔG are in units of eV. A positive ΔG is denoted with a -, indicating that the dissolution is not predicted to be favorable.

	Li-O		HO		H_2O	
	pH = 3	pH = 6	pH = 3	pH = 6	pH = 3	pH = 6
Ni	-0.58	-0.23	-1.94	-1.24	-1.08	-0.54
Co	-	-	-0.66	-	-	-
Mn	-	-	-	-	-	-

Decreasing Transition Metal Vacancy Density

One possible reason why Co and Mn dissolution from NMC_{h-H} is not favorable relative to Ni is that the surface TM vacancy density was too high for either to dissolve. As discussed in the Methodology section, to investigate a lower surface TM vacancy density, one needs to increase the size of the supercell slab. Here the size of the slab is increased from $2\sqrt{3} \times \sqrt{3}$ to $3\sqrt{3} \times \sqrt{3}$. The total number of surface transition metals increases from 6 to 9, so removal of one TM will result in a vacancy density of 11.1% (1/9).

For the larger supercell slabs, ΔG of dissolution of transition metals for a range of H-coverage from 1/3 to 2/3 is computed. In this series, coverage of 4/9 and 5/9 are also included to investigate the effects of hydration close to 1/2 surface coverage and because Li and H surface exchanges may not necessarily be stoichiometric in a dynamic system. Depicted in Figures 8a-8c, the overall trend in dissolution is Ni $>$ Co $>$ Mn, and the magnitude of ΔG is dependent upon surface H-coverage. Dissolution of all 3 TM, for all H-coverages between 1/3 and 2/3, is predicted to occur, but is more energetically favorable for higher H-coverages. This is variable and dependent upon pH; the slopes of ΔG are different from each other and the higher vacancy density of 16.7%. The change in free energy of dissolution of TM between surface coverages is larger at lower pH and smaller at higher pH. At lower pH it is more likely that TM will dissolve from the (001) surface, and at higher pH it is less likely that TM will dissolve. As pH increases beyond 9, removal of TM-OH is unlikely since the aqueous media may deprotonate the surface before OH can assist in dissolution. This suggests that aqueous syntheses need to take place at pH greater than those included here to

sidestep *TM* dissolution.

Decreasing the surface *TM* vacancy density from 16.7% to 11.1% has a larger impact on Co and Mn removal than it does on Ni. For example, at pH = 6 the difference between *TM*-OH removal for 16.6% (1/2 H coverage) and 11.1% (1/3 H coverage) vacancy densities is 0.86 eV for Ni and 1.43 and 1.54 eV for Co and Mn, respectively. The dissolution of Ni is less sensitive to surface terminations and *TM* vacancy density than either Co and Mn. Further support for this claim is that Ni dissolution from the NMC (001) surface is predicted to occur for *all* pH values, unlike Co and Mn. ΔG dissolution for all H-coverages investigated here, for both pH = 3 and pH = 6, are compared in Table 3. We interpret the driving force for dissolution of Ni as a consequence of its tendency to prefer square planar coordination as opposed to the octahedral environment of the delafossite structure type. A comparison of the PDOS for the vacancy structures is presented in Section 3 of the Supplemental Materials.

Li-Deficient Surface Terminations

In the previous sections of the Results, it was demonstrated that changes in the (001) surface termination will affect both the structure and electronic states of the *TM*, and this will have an impact of the likelihood of dissolution. Thus far the starting point for *all* dissolution cycles has been NMC_{h-Li}, a (001) NMC surface with 1/2 Li coverage. As mentioned in the Introduction, recent syntheses of NMC nanosheets show that for a range of NMC compositions, the overall lithiation state (x_{Li}) can vary $\approx$ between 1/3 and 2/3 (*59*, *61*), and that x_{Li} is synthesis dependent. Here we investigate the effects of a non-stoichiometric Li deficient surface as the starting point for ΔG of *TM* dissolution.

If the initial Li-deficient supercell slab has 1/3 Li coverage (NMC_{ot-Li}), computing *TM*-OH dissolution shows that ΔG increases by $\approx$ 3 eV for all TM, up to pH = 7. This means that Ni, Co, and Mn dissolution are only favorable until pH = 5.4, 3.8, and 1.4, respectively. Figure 8 compares ΔG dissolution for the three cations of a 2/3 H covered surface for whose reaction cycles start with either NMC_{h-Li} (solid lines) or NMC_{ot-Li} (dotted lines). The large change in ΔG for this

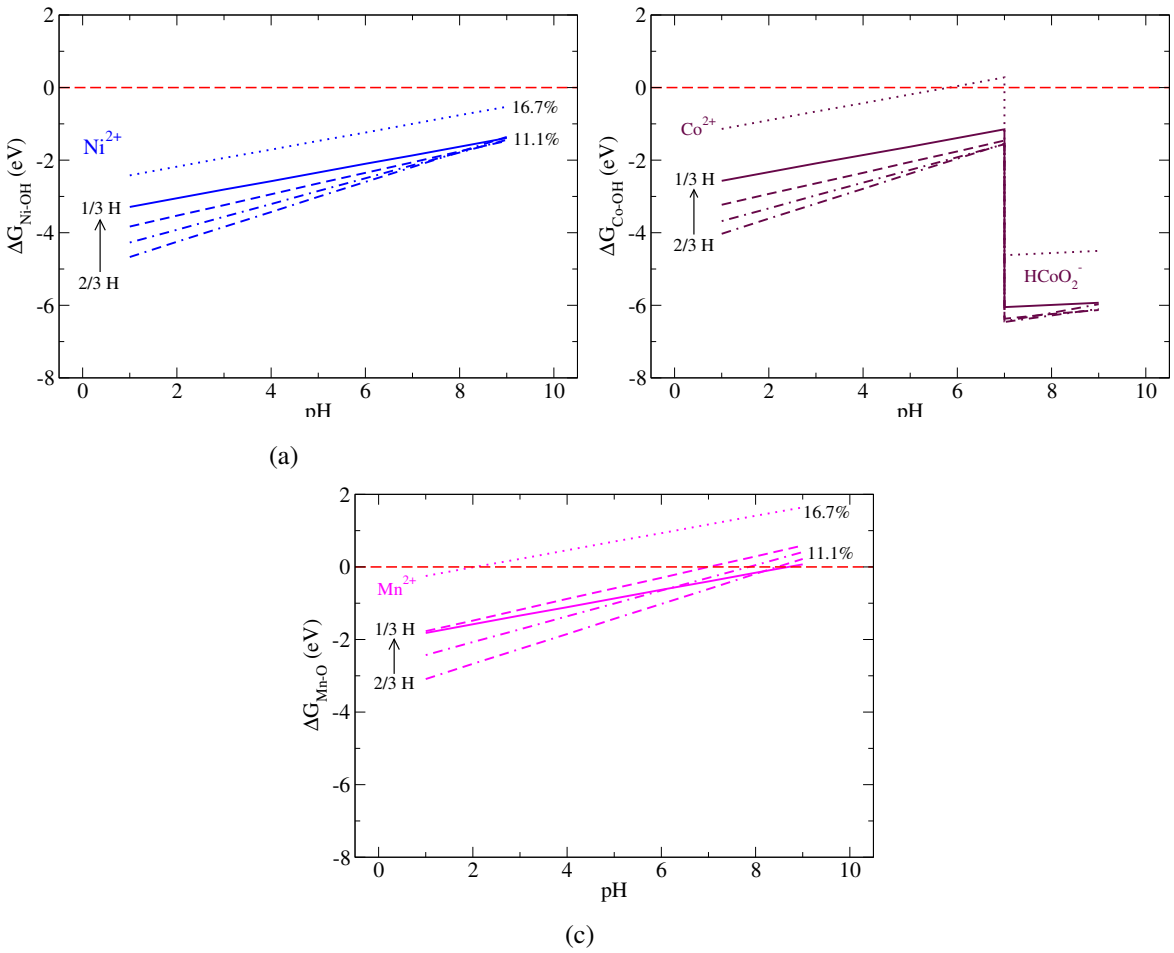

Figure 8: Shown here are comparison of TM-OH dissolution between $2\sqrt{3} \times \sqrt{3}$ (16.7% vacancy density, dotted lines) and $3\sqrt{3} \times \sqrt{3}$ (11.1% vacancy density, solid and dashed lines) supercell surface slabs. The 11.1% vacancy density surface slabs have between $\frac{1}{3}$ and $\frac{2}{3}$ H-coverage, for a) Ni b) Co c) Mn. Same color scheme as Figure 6.

process demonstrates that initial surface termination dictates the dissolution of cations in aqueous media. This comparison also implies that if the starting material is overall Li-deficient, the surface Li coverage may be closer to 1/2 than 1/3, otherwise not even Ni would be removed until pH 5.4 or below. Dissolution data for these tests are presented at the end of Table 3.

Environmental Implications

The present study helps fill the current knowledge gaps between molecular-level transformations of CMOs that take place at the nanoscale and their potential biological impact for a range of envi-

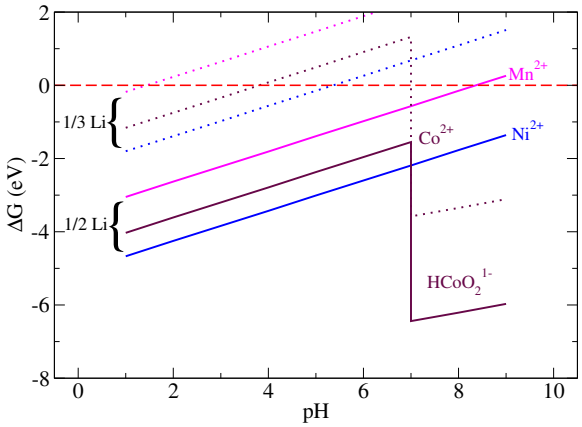

Figure 9: Shown here is a comparison of ΔG dissolution of 2/3 H-coverage supercell slabs for 2 different initial Li surface coverages of 1/2 and 1/3. Same color scheme as Figure 6.

Table 3: A comparison of ΔG of TM dissolution at 11.1% TM vacancy density for each of the H-coverages studied here. The last columns are for TM dissolution from the 2/3 H covered surface if the starting point were a Li-deficient surface. All ΔG are in units of eV. A positive ΔG is denoted with a -, indicating that the dissolution is not predicted to be favorable.

	1/3 H		4/9 H		5/9 H		2/3 H		2/3 H	
	pH = 3	pH = 6	pH = 3	pH = 6	pH = 3	pH = 6	pH = 3	pH = 6	pH = 3	pH = 6
Ni	-2.81	-2.10	-3.24	-2.35	-3.56	-2.50	-3.84	-2.60	-0.98	-
Co	-2.09	-1.39	-2.64	-1.76	-2.97	-1.92	-3.20	-1.96	-0.34	-
Mn	-1.28	-0.52	-1.18	-0.35	-1.68	-0.61	-2.22	-0.98	-	-

ronmentally relevant species and concentrations. Combining first-principles DFT calculations and solvent-ion thermodynamics is an effective method that can be used to elucidate the mechanistic pathways that lead to chemical transformations of CMOs for a wide range of conditions. For example, one can create DFT calculable speciation diagrams (*71*) for (meta)stable CMOs that take into account dynamic factors such as pH and concentration that yield insights into the molecular mechanistics of nanoparticle transformation. This information can be used to elucidate the possible transformations that take place for a range of conditions and in some cases, exclude possibilities that are not likely to occur for a given set of environmental or experimental conditions. As demonstrated here, this approach can yield atomistic insights into the reactive species and intermediates involved in complex chemical reactions and could serve as the input data to guide the redesign of current CMOs.

The molecular level understanding obtained from the study enables a chemical understanding of previously reported dissolution trends. This, combined with the evidence that cation leaching is a pathway to the negative biological impact of CMOs in the environment, points to possible design rules to explore in the development of sustainable nanotechnology. We predict that Ni dissolution from NMC will proceed for almost all environmental conditions investigated, while the dissolution of Co and Mn is highly dependent upon vacancy density and surface coverage. One route to mitigate the negative biological impact of NMC could be to (partially) substitute Ni for another redox active TM that is not toxic to a wide range of organisms. In comparing TM dissolution mediated by different surface species, we find that dissolution of TM-OH is preferred to dissolution of TM-H_2O for the range of pH investigated here. Since TM dissolution is indirectly mediated by surface exchange of Li and H, and we show that OH are required for dissolution, then our results suggests that a protective surface coating (*78–80*) that does not hydrolyze, and prevents Li exchange (to form surface OH), may be an attractive alternative to complete or partial Ni replacement. Some examples could be derived from small molecule adsorbates that exist in natural waters, such as sulfate or phosphate, ordered metal phosphate derivatives (*81*), or amorphous coatings such as LiPON (*82*).

The results of our first-principles investigations can be used as input datasets for curated databases such as the recently created Nanomaterial Data Curation Initiative (NDCI) (*83*). The field of nanoscience involves many scientific disciplines that generate a complex, diverse amount of information (*84*), so the NDCI takes an informatics approach to understanding nanomaterial behavior, where nanocuration is seen as a path forward to make informed decisions on nanomaterials through collaborative assessments and evaluations of the vast amounts of available data. These efforts are hindered by the lack of completeness and quality of nanomaterial data (*85*), the lack of material diversity (i.e, only properties of binary metal oxides and alloys), and that the development of hazard and risk profiles cannot keep up with the technological advancements made in the field of nanotechnology. Minimum nanomaterial characterization standards have been proposed, but not yet widely adopted. The methods presented here have the ability to predict the potential health

and environmental impact (*16*) in a systematic manner, and go beyond simple materials (*86*), since CMO are often multicomponent, complex mixtures.

Another area where the predictions presented here could have a sizable impact is in the improvement of environmental fate models (*19*, *87*). These models forecast the effects of releasing materials into naturally occurring systems (*88*), and until recently, the input parameters for these models have largely belonged to either bulk materials or "as-synthesized" nanoparticles, which do not take into account the possible transformations that an CMO may undergo. It has also been put forth that stream dynamics studies (*89*) under-predict nanoparticle mobility and reactivity and posit that CMO will not be found in their as-synthesized state, thereby undercutting the benefit of these models.

Associated Content

Supporting Information. Thermodynamics of the DFT + solvent ion method. Dissolution comparison using DFT + U methodology.

Author Information

Corresponding Author: sara-mason@uiowa.edu

Notes: The authors declare no competing financial interest.

Acknowledgements

This work was supported by National Science Foundation Center for Chemical Innovation Program grant CHE-1503408 for the Center for Sustainable Nanotechnology. This research was supported in part through computational resources provided by The University of Iowa, Iowa City, Iowa and the National Science Foundation grant CHE-0840494. This work used the Extreme Science

and Engineering Discovery Environment (XSEDE (*90*)), which is supported by National Science Foundation grant number ACI-1548562. The authors thank Profs. Christy Haynes, Qiang Cui and Rigoberto Hernandez for useful discussions of this work.

References

(1) Hamers, R. J. Nanomaterials and Global Sustainability. *Acc. Chem. Res.* **2017**, *50*, 633–637.

(2) Lim, S. Y.; Shen, W.; Gao, Z. Carbon Quantum Dots and Their Applications. *Chem. Soc. Rev.* **2015**, *44*, 362–381.

(3) Murphy, C. J.; Vartanian, A. M.; Geiger, F. M.; Hamers, R. J.; Pedersen, J.; Cui, Q.; Haynes, C. L.; Carlson, E. E.; Hernandez, R.; Klaper, R. D.; Orr, G.; Rosenzweig, Z. Biological Responses to Engineered Nanomaterials: Needs for the Next Decade. *ACS Cent. Sci.* **2015**, *1*, 117–123.

(4) Lu, J.; Chen, Z.; Ma, Z.; Pan, F.; Curtiss, L. A.; Amine, K. The role of nanotechnology in the development of battery materials for electric vehicles. *Nature Nanotech.* **2016**, *11*, 1031–1038.

(5) Ellingsen, L. A.-W.; Hung, C. R.; Majeau-Bettez, G.; Singh, B.; Chen, Z.; Whittingham, M. S.; Stromman, A. H. Nanotechnology for environmentally sustainable electromobility. *Nature Nanotech.* **2016**, *11*, 1039–1051.

(6) Larcher, D.; Tarascon, J.-M. Towards greener and more sustainable batteries for electrical energy storage. *Nature Chem.* **2014**, *7*, 19–29.

(7) Sani-Kast, N.; Labille, J.; Ollivier, P.; Slomberg, D.; Hungerbuhler, K.; Scheringer, M. A network perspective reveals decreasing material diversity in studies on naoparticle interactions with dissolved organic matter. *PNAS* **2017**, *114*, E1756–E1765.

(8) Notter, D. A.; Gauch, M.; Widmer, R.; Wager, P.; Stamp, A.; Zah, R.; Althaus, H. J. Contribution of Li-ion Batteries to the Environmental Impact of Electric Vehicles. *Environ. Sci. Technol.* **2010**, *44*, 6550–6556.

(9) Zhang, K.; Schnoor, J. L.; Zeng, E. Y. E-Waste Recycling: Where Does It Go from Here? *Environ. Sci. Technol.* **2012**, *46*, 10861–10867.

(10) Maurer-Jones, M. A.; Gunsolus, I. L.; Murphy, C. J.; Haynes, C. L. Toxicity of Engineered Nanoparticles in the Environment. *Anal. Chem.* **2013**, *85*, 3036–3049.

(11) Lopez-Serrano, A.; Olivas, R. M.; Landaluze, J. S.; Camara, C. Nanoparticles: A Global Vision. Characterization, Separation, and Auantification Methods. Potential Environmental and Health Impact. *Anal. Chem.* **2014**, *6*, 38–56.

(12) Gunsolus, I. L.; Haynes, C. L. Analytical Aspects of Nanotoxicology. *Anal. Chm.* **2016**, *88*, 451–479.

(13) Xia, T. et al. Decreased Dissolution of ZnO by Iron Doping Yields Nanoparticles with Reduced Toxicity in the Rodent Lung and Zebrafish Embryos. *ACS Nano* **2011**, *5*, 1223–1235.

(14) Manshian, B. B.; Pokhrel, S.; Himmelreich, U.; Tamm, K.; Sikk, L.; Fernandez, A.; Rallo, R.; Tamm, T.; Madler, L.; Soenen, S. J. In Silico Design of Optimal Dissolution Kinetics of Fe-Doped ZnO Nanoparticles Results in Cancer-Specific Toxicity in a Preclinical Rodent Model. *Adv. Healthcare Mater.* **2017**, *6*, 1001379–1–11.

(15) Naatz, H.; Lin, S.; Li, R.; Jiang, W.; Ji, Z.; Chang, C.-H.; Koser, J.; Thoming, J.; Xia, T.; Nel, A. E.; Madler, L.; Pokhrel, S. Safe-by-Design CuO Nanoparticles via Fe-Doping, Cu-O Bond Length Variation, and Biological Assessment in Cells and Zebrafish. *ACS Nano* **2017**, *11*, 501–515.

(16) Gilbertson, L. M.; Zimmerman, J. B.; Plata, D. L.; Hutchinson, J. E.; Anastas, P. T. Designing

nanomaterials to maximize performance and minimize undesirable implications guided by the Principles of Green Chemistry. *Chem. Soc. Rev.* **2015**, *44*, 5758–5777.

(17) Zhang, H.; Chen, B.; Banfield, J. F. Particle Size and pH Effects on Nanoparticle Dissolution. *J. Phys. Chem. C.* **2010**, *114*, 14876–14884.

(18) Ma, S.; Zhou, K.; Yang, K.; Lin, D. Heteroagglomeration of Oxide Nanoparticles with Algal Cells: Effects of Particle Type, Ionic Strength and pH. *Environ. Sci. Technol.* **2015**, *49*, 932–939.

(19) Lowry, G. V.; Gregory, K. B.; Apte, S. C.; Lead, J. R. Transformations of Nanomaterials in the Environment. *Environ. Sci. Technol.* **2012**, *46*, 6893–6899.

(20) Mudunkotuwa, I. A.; Grassian, V. H. Biological and environmental media control oxide nanoparticle surface composition: the roles of biological components (proteins and amino acids), inorganic oxyanions and humic acid. *Environ. Sci. Nano.* **2015**, *2*, 429–439.

(21) Grassian, V. H. et al. NanoEHS - defining fundamental science needs: no easy feat when the simple itself is complex. *Environ. Sci.: Nano.* **2016**, *3*, 15–27.

(22) Zhou, F.; Cococcioni, M.; Marianetti, C. A.; Morgan, D.; Ceder, G. First-Principles Prediction of Redox Potentials in Transition-Metal Compounds with LDA+U. *Phys. Rev. B* **2004**, *70*, 235121–1–8.

(23) Aykol, M.; Kim, S.; Wolverton, C. van der Waals Interactions in Layered Lithium Cobalt Oxides. *J. Phys. Chem. C* **2015**, *119*, 19053–19058.

(24) Hautier, G.; Jain, A.; Ong, S. P.; Kang, B.; Moore, C.; Doe, R.; Ceder, G. Phosphates as Lithium-Ion Battery Cathodes: An Evaluation Based on High-throughput *ab initio* Calculations. *Chem. Mater.* **2011**, *23*, 3495–3508.

(25) Hautier, G.; Jain, A.; Chen, H.; Moore, C.; Ong, S. P.; Ceder, G. Novel Mixed Polyanions

Lithium-Ion Battery Cathode Materials Predicted by High-Throughput *ab initio* Calculations. *J. Mater. Chem.* **2011**, *21*, 17147–17153.

(26) Urban, A.; Matts, I.; Abdellahi, A.; Ceder, G. Computational Design and Preparation of Cation-Disordered Oxides for High-Energy-Density Li-Ion Batteries. *Adv. Energy Mater.* **2016**, *6*, 1600488–1–8.

(27) Yoon, W.-S.; Balasubramanian, M.; Chung, K.-Y.; Yang, X.-Q.; McBreen, J.; Grey, C. P.; Fischer, D. A. Investigation of the Charge Compensation Mechanism on the Electrochemically Li-Ion Deintercalated $Li_{1-x}Co_{1/3}Ni_{1/3}Mn_{1/3}O_2$ Electrode System by Combination of Soft and Hard X-ray Absorption Spectroscopy. *J. Am. Chem. Soc.* **2005**, *127*, 17479–17487.

(28) Koyama, Y.; Yabuuchi, N.; Tanaka, I.; Adachi, H.; Ohzuku, T. Solid State Chemistry and Electrochemistry of $LiCo_{1/3}Ni_{1/3}Mn_{1/3}O_2$ for Advanced Lithium-Ion Batteries. *J. ELectrochem. Soc.* **2004**, *151*, A1545–A1551.

(29) Luo, G.; Zhao, J.; Ke, X.; Zhang, P.; Sun, H.; Wang, B. Structure, Electrode Voltage and Activation Energy of $LiMn_xCo_yNi_{1-x-y}O_2$ Solid Solutions as Cathode Materials for Li Batteries from First-Principles. *J. Electrochem. Soc.* **2012**, *159*, A1203–A1208.

(30) Dolotko, O.; Senyshyn, A.; Muhlbauer, M. J.; Nikolowski, K.; Ehrenberg, H. Understanding structural changes in NMC Li-ion cells by *in situ* neutron diffraction. *J. Power Sources* **2014**, *255*, 197–203.

(31) Lee, J.; Urban, A.; Li, X.; Su, D.; Hautier, G.; Ceder, G. Unlocking the Potential of Cation-Disordered Oxides for Rechargeable Lithium Batteries. *Science* **2014**, *343*, 519–522.

(32) Moradabadi, A.; Kaghazchi, P. Mechanism of Li Intercalation/Deintercalation into/from the Surface of $LiCoO_2$. *Phys.Chem.Chem.Phys.* **2015**, *17*, 22917–22922.

(33) Dixit, M.; Kosa, M.; Lavi, O. S.; Markovsky, B.; Aurbach, D.; Major, D. T. Thermodynamic

and kinetic studies of $LiNi_{0.5}Co_{0.2}Mn_{0.3}O_2$ as a positive electrode material for Li-ion batteries using first-principles. *Phys. Chem. Chem. Phys.* **2016**, *18*, 6799–6812.

(34) Goodenough, J. B.; Kim, Y. Challenges for Rechargeable Li Batteries. *Chem. Mater.* **22**, *2010*, 587–603.

(35) Dunn, B.; Kamath, H.; Tarascon, J.-M. Electrical ENergy Storage for the Grid: A Battery of Choices. *Science* **2011**, *334*, 928–935.

(36) Choi, N. S.; Chen, Z.; Freunberger, S. A.; Ji, X.; Sun, Y. K.; Amine, K.; Yushin, G.; Nazar, L. F.; Cho, J.; Bruce, P. G. Challenges Facing Lithium Batteries and ELectrical Double Layer Capacitors. *Angew. Chem. Int. Ed.* **2012**, *51*, 9994–10024.

(37) Goodenough, J. B.; Park, K.-S. The Li-Ion Rechargeable Battery: A Perspective. *J. Am. Chem. Soc.* **2013**, *135*, 1167–1176.

(38) Nitta, N.; Wu, F.; Lee, J.-T.; Yushin, G. Li-ion battery materials: present and future. *Mater. Today* **2015**, *18*, 252–264.

(39) Ceder, G.; Chiang, Y.-M.; Sadoway, D. R.; Aydinol, M. K.; Jang, Y.-I.; Huang, B. Identification of Cathode Materials for Lithium Batteries Guided by First-Principles Calculations. *Nature* **1998**, *392*, 694–696.

(40) Carlier, D.; derVen, A. V.; Delmas, C.; Ceder, G. First-Principles Investigation of Phase Stability in the O_2-$LiCoO_2$ System. *Chem. Mater.* **2003**, *15*, 2651–2660.

(41) Hwang, B. J.; Tsai, Y. W.; Carlier, D.; Ceder, G. A Combined Computational/Experimental Study on $LiNi_{1/3}Co_{1/3}Mn_{1/3}O_2$. *Chem. Mater.* **2003**, *15*, 3676–3682.

(42) Kramer, D.; Ceder, G. Tailoring the Morphology of $LiCoO_2$: A First Principles Study. *Chem. Mater.* **2009**, *21*, 3799–3809.

(43) Islam, M. S.; Fischer, C. A. J. Lithium and Sodium Battery Cathode Materials: Computational Insights into Voltage, Diffusion and Nanostructural Properties. *Chem. Soc. Rev.* **2014**, *43*, 185–204.

(44) Urban, A.; Seo, D.-H.; Ceder, G. Computational understanding of Li-ion batteries. *NPJ Computational Mater.* **2016**, *2*, 16002–1–13.

(45) Jain, A.; Shin, Y.; Persson, K. Computational predictions of energy materials using density functional theory. *Nature Review Materials* **2016**, *1*, 1–13.

(46) Cococcioni, M. Accurate and Efficient Calculations on Strongly Correlated Minerals with the LDA + *U* Method: Review and Perspectives. *Rev. in Mineral. and Geochem.* **2010**, *71*, 147–167.

(47) Bennett, J. W.; Garrity, K. F.; Rabe, K. M.; Vanderbilt, D. Hexagonal *ABC* Semiconductors as Ferroelectrics. *Phys. Rev. Lett.* **2012**, *109*, 167602.

(48) Bennett, J. W.; Garrity, K. F.; Rabe, K. M.; Vanderbilt, D. Orthorhombic *ABC* Semiconductors as Antiferroelectrics. *Phys. Rev. Lett.* **2013**, *110*, 017603.

(49) Huang, X.; Ramadugu, S. K.; Mason, S. E. Surface-Specific DFT + *U* Approach Applied to α-Fe_2O_3 (0001). *J. Phys. Chem. C* **2016**, *120*, 4919–4930.

(50) Rong, X.; Kolpak, A. M. Ab initio Approach for Prediction of Oxide Surface Structure, Stoichiometry, and Electrocatalytic Activity in Aqueous Solution. *Phys. Chem. Lett.* **2015**, *6*, 1785–1789.

(51) Huang, X.; Bennett, J. W.; Hang, M. N.; Laudadio, E. D.; Hamers, R. J.; Mason, S. E. *Ab initio* Atomistic Thermodynamics Study of the (001) Surface of $LiCoO_2$ in a Water Environment and Implications for Reactivity under Ambient Conditions. *J. Phys. Chem. C.* **2017**, *121*, 5069–5080.

(52) Dogangun, M.; Hang, M. N.; Troiano, J. M.; McGeachy, A. C.; Melby, E. S.; Pedersen, J. A.; Hamers, R. J.; Geiger, F. M. Alteration of Membrane Compositional Asymmetry by $LiCoO_2$ Nanosheets. *ACS Nano* **2015**, *9*, 8755–8765.

(53) Dogangun, M.; Hang, M. N.; Machesky, J.; Hamers, R. J.; Geiger, F. M. Evidence for Considerable Metal Cation Concentrations from Li Intercalation Compounds in the Nano-Bio Interface Gap. *J. Phys. Chem. C.* **2017**, *121*, 27473–27482.

(54) Poizot, P.; Laruelle, S.; Grugeon, S.; Dupont, L.; Tarascon, J. M. Nano-Sized Transition-Metal Oxides as Negative-Electrode Materials for Lithium-Ion Batteries. *Nature* **2000**, *407*, 496–499.

(55) Kang, K.; Meng, Y. S.; Breger, J.; Grey, C. P.; Ceder, G. Electrodes with High Power and High Capacity for Rechargeable Lithium Batteries. *Science* **2006**, *311*, 977–980.

(56) Belharouak, I.; Sun, Y. K.; Liu, J.; Amine, K. $Li(Ni_{1/3}Co_{1/3}Mn_{1/3})O_2$ as a Suitable Cathode for High Power Applications. *J. Power Sources* **2003**, *123*, 247–252.

(57) Conry, T. E.; Mehta, A.; Cabana, J.; Doeff, M. M. Structural Underpinnings of the Enhanced Cycling Stability upon Al-Substitution in $LiNi_{0.45}Mn_{0.45}Co_{0.1-y}Al_yO_2$ Positive Electrode Materials for Li-ion Batteries. *Chem. Mater.* **2012**, *24*, 3307–3317.

(58) Li, Z.; Ban, C.; Chernova, N. A.; Wu, Z.; Upreti, S.; Dillon, A.; Whittingham, M. S. Towards understanding the rate capability of layered transition metal oxides $LiNi_yMn_yCo_{1-2y}O_2$. *J. Power Sources* **2014**, *268*, 106–112.

(59) Hang, M. N.; Gunsolus, I. L.; Wayland, H.; Melby, E. S.; Mensch, A. C.; Hurley, K. R.; Pedersen, J. A.; Haynes, C. L.; Hamers, R. J. Impact of Nanoscale Lithium Nickel Manganese Cobalt Oxide (NMC) on the Bacterium Shewanella oneidensis MR-1. *Chem. Mater.* **2016**, *28*, 1092–1100.

(60) Bozich, J.; Hang, M.; Hamers, R. J.; Klaper, R. Core chemistry influences the toxicity of multicomponent metal oxide nanomaterials, lithium nickel manganese cobalt oxide, and lithium cobalt oxide to *Daphnia magna*. *Environ. Toxicology and Chem.* **2017**, *36*, 2493–2502.

(61) Gunsolus, I. L.; Hang, M. N.; Hudson-Smith, N. V.; Buchman, J. T.; Bennett, J. W.; Conroy, D.; Mason, S. E.; Hamers, R. J.; Haynes, C. L. Influence of nickel manganese cobalt oxide nanoparticle composition on toxicity toward *Shewanella oneidensis* MR-1: redesigning for reduced biological impact. *Environ. Sci.: Nano.* **2017**, *4*, 636–646.

(62) Hohenberg, P.; Kohn, W. Inhomogeneous Electron Gas. *Phys. Rev.* **1964**, *136*, B864–71.

(63) Kohn, W.; Sham, L. J. Self-Consistent Equations Including Exchange and Correlation Effects. *Phys. Rev.* **1965**, *140*, A1133–8.

(64) Giannozzi, P.; Baroni, S.; Bonini, N.; Calandra, M.; Car, R.; Cavazzoni, C.; Ceresoli, D.; Chiarotti, G. L.; Cococcioni, M.; Dabo, I.; et al., Quantum ESPRESSO: A Modular and Open-Source Software Project for Quantum Simulations of Materials. *J. Phys.:Condens. Matter* **2009**, *21*, 395502–20.

(65) Vanderbilt, D. Soft Self-Consistent Pseudopotentials in a Generalized Eigenvalue Formalism. *Phys. Rev. B Rapid Comm.* **1990**, *41*, 7892–5.

(66) Garrity, K. F.; Bennett, J. W.; Rabe, K. M.; Vanderbilt, D. Pseudopotentials for high-throughput DFT calculations. *Comp. Mater. Sci.* **2014**, *81*, 446–452.

(67) Perdew, J. P.; Burke, K.; Ernzerhof, M. Generalized Gradient Approximation Made Simple. *Phys. Rev. Lett.* **1996**, *77*, 3865–8.

(68) Monkhorst, H. J.; Pack, J. D. Special Points for Brillouin-Zone Integrations. *Phys. Rev. B* **1976**, *13*, 5188–5192.

(69) Rong, X.; Parolin, J.; Kolpak, A. M. A Fundamental Relationship between Reaction Mechanism and Stability in Metal Oxide Catalysts for Oxygen Evolution. *ACS Catal.* **2016**, *6*, 1153–1158.

(70) Wagman, D. D. E.; Halow, I.; Parker, V. B.; Bailey, S. M.; Schumm, R. H. Selected Values of Chemical Thermodynamic Properties. *National Bureau of Standards* **1971**,

(71) Persson, K. A.; Waldwick, B.; Lazic, P.; Ceder, G. Prediction of solid-aqueous equilibria: Scheme to combine first-principles calculations of solids with experimental aqueous states. *Phys. Rev. B.* **2012**, *85*, 235438.

(72) Hubbard, J. Electron Correlation in Narrow Energy Bands. *Proc. R. Soc. Lond. A* **1963**, *276*, 238–257.

(73) Anisimov, V. I.; Gunnarsson, O. Density-Functional Calculation of Effective Coulomb Interactions in Metals. *Phys. Rev. B.* **1991**, *43*, 7570.

(74) Anisimov, V. I.; Aryasetiawan, F.; Lichtenstein, A. I. First-principles Calculations of the Electronic Structure of Strongly Correlated Systems: the LDA + *U* Method. *J. Phys. Cond. Matter* **1997**, *9*, 767.

(75) Shick, A. B.; Liechtenstein, A. I.; Pickett, W. E. Implementation of the LDA+U method using the full-potential linearized augmented plane-wave basis. *Phys. Rev. B* **1999**, *60*, 10763–9.

(76) Yabuuchi, N.; Ohzuku, T. Novel lithium insertion material of $LiCo_{1/3}Ni_{1/3}Mn_{1/3}O_2$ for advanced lithum-ion batteries. *J. Power Sources* **2003**, *119-121*, 171–174.

(77) Yin, S.-C.; Rho, Y.-H.; Swainson, I.; Nazar, L. F. X-ray/Neutron Diffraction and Electrochemical Studies of Lithium De/Re-Intercalation in $Li_{1-x}Co_{1/3}Ni_{1/3}Mn_{1/3}O_2$ (x= 0 to 1). *Chem. Mater.* **2006**, *18*, 1901–1910.

(78) Cho, J.; Lee, J.-G.; Kim, B.; Park, B. Effect of P_2O_5 and $AlPO_4$ Coating on $LiCoO_2$ Cathode Material. *Chem. Mater.* **2003**, *15*, 3190–3193.

(79) Kim, J.; Noh, M.; Cho, J.; Kim, H.; Kim, K.-B. Controlled Nanoparticle Metal Phosphates (*M*= Al, Fe, Ce, and Sr) Coatings on $LiCoO_2$ Cathode Materials. *J. Electrochem. Soc.* **2005**, *152*, A1142–A1148.

(80) Verdier, S.; Ouatani, L. E.; Dedryvere, R.; Bonhomme, F.; Biensan, P.; Gonbeau, D. XPS Study on Al_2O_3- and $AlPO_4$-Coated $LiCoO_2$ Cathode Material for High-Capacity Li-Ion Batteries. *J. Electrochem. Soc.* **2007**, *154*, A1088–A1099.

(81) Taminato, S.; Hirayama, M.; Suzuki, K.; Tamura, K.; Minato, T.; Arai, H.; Uchimoto, Y.; Ogumi, Z.; Kanno, R. Lithium Intercalation and Structural Changes at the $LiCoO_2$ Surface under High Voltage Battery Operation. *J. Power Sources* **2016**, *307*, 599–603.

(82) Kim, Y.; Veith, G. M.; Nanda, J.; Unocic, R. R.; Chi, M.; Dudney, N. J. High Voltage Stability of $LiCoO_2$ Particles with a Nanoscale Lipon Coating. *Electrochim. Acta.* **2011**, *56*, 6573–6580.

(83) Hendren, C. O.; Powers, C. M.; Hoover, M. D.; Harper, S. L. The Nanomaterial Data Curation Initiative: A collaborative approach to assessing, evaluating, and advancing the state of the field. *Beilstein J. Nanotechnol.* **2015**, *6*, 1752–1762.

(84) Powers, C. M.; Mills, K. A.; Morris, S. A.; Klaessig, F.; Gaheen, S.; Lewinski, N.; Hendren, C. O. Nanocuration workflows: Establishing best practices for identifying, inputting, and sharing data to inform decisions on nanomaterials. *Beilstein J. Nanotechnol.* **2015**, *6*, 1860–1871.

(85) Robinson, R. L. M. et al. How should the completeness and quality of curated nanomaterial data be evaluated? *Nanoscale* **2016**, *8*, 9919.

(86) Cui, Q.; Hernandez, R.; Mason, S. E.; Frauenheim, T.; Pedersen, J. A.; Geiger, F. Sustainable Nanotechnology: Opportunities and Challenges for Theoretical/Computational Studies. *J. Phys. Chem. B* **2016**, *120*, 7297–7306.

(87) Levard, C.; Hotze, E. M.; Lowry, G. V.; G. E. Brown, J. Environmental Transformations of Silver Nanoparticles: Impact on Stability and Toxicity. *Environ. Sci. Technol.* **2012**, *46*, 6900–6914.

(88) Dale, A. L.; Casman, E. A.; Lowry, G. V.; Lead, J. R.; Viparelli, E.; Baalousha, M. Modeling Nanomaterial Environmental Fate in Aquatic Systems. *Environ. Sci. Technol.* **2015**, *49*, 2587–2593.

(89) Dale, A. L.; Lowry, G. V.; Casman, E. A. Stream Dynamics and Chemical Transformations Control the Environmental Fate of Silver and Zinc Oxide Nanoparticles in a Watershed-Scale Model. *Environ. Sci. Technol.* **2015**, *49*, 7285–7293.

(90) Towns, J.; Cockerill, T.; Dahan, M.; Foster, I.; Gaither, K.; Grimshaw, A.; Hazlewood, V.; Lanthrop, S.; Lifka, D.; Peterson, G. D.; Roskies, R.; Scott, J. R.; Wilkins-Diehr, N. XSEDE:Accelerating Scientific Discovery. *Comp. Sci. Engineering* **2014**, *16*, 62–74.

TOC Entry